Received: 11 December 2018 | Revised: 4 March 2019 | Accepted: 9 April 2019

DOI: 10.1111/jace.16495

Journal of the American Ceramic Society

ORIGINAL ARTICLE

The modification of surface, size and shape of barium zirconate powder *via* salt flux

Thitirat Charoonsuk[1] | **Taras Kolodiazhnyi**[2] | **Naratip Vittayakorn**[1,3]

[1]Advanced Materials Research Unit, Faculty of Science, King Mongkut's Institute of Technology Ladkrabang, Bangkok, Thailand

[2]National Institute for Materials Science, Tsukuba, Japan

[3]Department of Chemistry, Faculty of Science, King Mongkut's Institute of Technology Ladkrabang, Bangkok, Thailand

Correspondence
Naratip Vittayakorn, Advanced Materials Research Unit, Faculty of Science, King Mongkut's Institute of Technology Ladkrabang, Bangkok, Thailand.
Email: naratip.vi@kmitl.ac.th

Funding information
National Institute for Materials Science, Grant/Award Number: PA4020 and PA5160 ; King Mongkut's Institute of Technology Ladkrabang, Grant/Award Number: 2562-01-05-46 and A118-0361-005 ; Academic Melting-Pot, Grant/Award Number: KREF146201 and KREF206203

Abstract

The "top-down" process *via* direct conversion of the micro (μm)-to-submicroscale (*sub*-μm) particle was applied in this work by using eutectic chloride salts to prepare $BaZrO_3$. The particle size at optimum condition could be decreased by more than 10 times from 2.1 ± 0.9 μm to 168 ± 23 nm without destroying the 1:1 of Ba:Zr stoichiometry. The uniform *sub*-μm-$BaZrO_3$ powder was sintered in order to obtain ~98% dense ceramic at 1400°C/10 h, which is significantly lower than the 1650°C in normal cases. The microwave dielectric constant, tan δ, and quality factor were also determined. Furthermore, this method also was applied to lead-free piezoelectric material in the $0.87BaTiO_3$–$0.13BaZrO_3$–$CaTiO_3$ (0.87BT–0.13BZ–CT) system. The particle size of 0.87BT–0.13BZ–CT was reduced greatly from >10 μm to 2.8 ± 0.4 μm. It can be proved that salt flux dissolution method enables high-purity with uniform sub-micro/nanometer powder production in one step by using simple laboratory equipment and low-cost raw materials.

KEYWORDS

$BaZrO_3$, microwave dielectric ceramic, nanoparticles, salt-flux dissolution

1 | INTRODUCTION

Nano/sub-microscale (*sub*-μm) fine powder of barium zirconate ($BaZrO_3$; BZ) and its derivatives are of considerable interest in many devices related to applications such as microwave dielectrics,[1] H_2 gas sensors,[2] protonic conductors in SOFCs,[3,4] ceramic capacitors in wireless communications,[5] and buffer layers for coated conductors,[6] since their optimum properties have been reached by controlling the shape, size, and crystal structure of powder source from the beginning.[7,8] Using fine powder also can improve sinterability, thus allowing the production of thin and dense ceramics, which are essential for obtaining high-performance ceramic crucibles for single-crystal growth,[9] Much effort has been made in developing synthetic strategies that have control over composition and morphologies. Small-sized, uniform shaped, and aggregate-free particles have always been the top priority in all cases of synthesizing.

"Bottom-up" strategies *via* solution-based routes have been in focus since they offer relatively better compositional and morphological control than the solid-state reaction, which yields hard-agglomerated powders with chemical inhomogeneity and undesirable morphology that has broadly dispersed particle sizes.[10,11] Various solution techniques such as simple reflux,[12] co-precipitation *via* oxalate[13,14] and citrate[15] routes, solution combustion,[16,17] and hydrothermal,[18] solvotherma[19] and sol-gel[20,21] processes have been explored. Co-precipitation is easier than other solution methods, which can produce the crystalline $BaZrO_3$ phase at temperatures mostly lower than 500°C. Nevertheless, presence of the $BaCO_3$ and ZrO_2 by-product, of up to 5%-10 wt%, is a common problem.[13–15] The use of urea or glycine as a reducing agent in combustion

solution permits a single-step synthesis that initiates the $BaZrO_3$ phase. Unfortunately, the calcination process is still required for completing the crystalline phase that generally provides an irregular morphology with large micron-sized particle products.[16,17] Desirable shape and size of the $BaZrO_3$ particle could be achieved directly from the direct reaction of precursor ions in strong basic solution *via* hydrothermal and solvothermal methods.[18] However, more uniform particles were developed by using complex organic ligands in order to prevent particle agglomeration in the solvothermal method.[19] Nevertheless, both of these methods required a long reaction time, and they suffered from difficult up-scaling in terms of high yield. Acceleration of the nucleation rate can be realized with a high degree of supersaturation in supercritical water, thus providing higher crystallinity with uniform particle size distribution, but this synthetic process has to be done with expensive equipment and a difficult operational system.[22,23] The sol-gel synthesis method is a powerful one for obtaining more homogeneous powder products.[24,25] The complex isopropoxide [$M(OiPr)_2$, M = Ba, Zr and iPr = $CH(CH_3)_2$] framework was synthesized from metal precursors before calcination of the hydrolyzed gel at >400°C in order to remove organic traces. Although the sol-gel process shows outstanding control of tiny and uniform particles (~10–50 nm), it also requires the use of highly purified precursors in complicated experiments and long synthesis times. Ultrafine powders have been achieved through modified solution techniques such as microwave-hydrothermal[26] and microwave solvothermal methods,[27] sol-gel combustion,[28] and the sol-gel hydrothermal technique.[29] However, precise control in obtaining a highly monodispersed particles, together with accurate stoichiometry, is fundamentally difficult because the solubility of Ba and Zr metal ions is totally different during the particle growth in solution.[19,30] Most of the extra steps can introduce a serious problem if any contamination or loss of Ba:Zr ratio occurs.[30]

Among the solution methods developed so far, recent publications from these authors also proposed sonochemical[31,32] and soft-mechanochemical methods,[33] in which calcination or heat treatment was unnecessary. It seems that smart techniques fulfill the characteristic requirements for synthesizing the extreme nm-$BaZrO_3$ fine powders. However, both processes need specific equipment, which is expensive and inconvenient. The limitations in all solution methods motivate these authors to find a technique that can produce the sub-microscale and nanoscale $BaZrO_3$ fine powder directly and also be consistent with industrial requirements, reproducibility, and cost.

Recent reports inspired a digestive ripening process that involved refluxing poly-dispersed bulk precursors within an excess solution of metallo-organic complex capping agents, such as hexadecyl-trimethyl-ammonium bromide (CTAB), tetraoctyl-ammonium bromide (TOAB), hexadecylamine (HDA), etc. Etched out metals, metal sulfides, and magnetic nanoparticles formed as clusters, resulting in precursor size reduction.[34–37] These authors previously published the way of obtaining a uniform $BaTiO_3$ nanoscale particles from microscale conversion using NaCl salt.[38] A variation in time and temperature provides great thermodynamical control over particle morphology, size, and size distribution. The conversion process was performed successfully without destroying the stoichiometric composition or crystal structure, which is the characteristic of this method.

The size and shape modification of $BaZrO_3$ and more complex oxide $0.87BaTiO_3$–$0.13BaZrO_3$–$CaTiO_3$ lead-free piezoelectric material was carried out in this study. Detailed characterization and structural analysis were performed by X-ray diffraction (XRD), Rietveld refinement, scanning electron microscopy (SEM), and SEM-energy dispersive X-ray (EDX) techniques in order to elucidate phase stabilization, particle morphology, and size within the eutectic salt reaction field. The optical property was studied by UV-Vis absorption and photoluminescence spectroscopy. The uniform *sub*-μm-$BaZrO_3$ powder product also was sintered in order to obtain dense ceramic as expected for application as a microwave dielectric. This study proved that the salt flux can be used to modify the surface, shape, and size of the functional complex oxide ceramics without the distortion of the stoichiometry.

2 | EXPERIMENTAL SECTION

2.1 | Materials

Barium carbonate ($BaCO_3$; >98.5% purity, purchased from Sigma Aldrich Co., Ltd., USA) and zirconium dioxide (ZrO_2; >99.0% purity, purchased from Riedel-de Haën Co., Ltd., Germany) were used as the starting precursor for preparing $BaZrO_3$ micron-size powders by solid-state reaction. Calcium carbonate ($CaCO_3$; >98.5% purity, purchased from Riedel-de Haën Co., Ltd., Germany) and titanium dioxide (TiO_2 > 99.0% purity, purchased from Sigma Aldrich Co., Ltd., USA) were used as the starting precursor with $BaCO_3$ and ZrO_2 for preparing $BaTiO_3$–$BaZrO_3$–$CaTiO_3$ micron-size powders by solid-state reaction. Sodium chloride (NaCl; >99.0% purity) and potassium chloride (KCl; >99.0% purity), both produced by Carlo Erba Reagents Co., Ltd., France, were used as a salt flux in the dissolution process.

2.2 | Salt flux dissolution method for converting $BaZrO_3$ micrometer to uniform submicron-powder

The irregular shape and non-uniform particles of μm-$BaZrO_3$ were used as a precursor in this work. Solid state reaction method was selected to prepare the μm-$BaZrO_3$ precursor. Barium carbonate ($BaCO_3$) and zirconium dioxide (ZrO_2)

were mixed according to the stoichiometry by 24 hours ball milling and calcined at 1300°C for 4 hours. After calcination, the μm-$BaZrO_3$ precursor was ground together with sodium chloride (NaCl) and potassium chloride (KCl) salts in a mortar for 15 minutes at a weight ratio of 1:25:25. The mixture was then placed in a covered alumina crucible and heated at various temperatures of 900°C-1200°C, with soaking times of 3-72 hours in air and a heating-cooling rate of 5°C/min. After the furnace had cooled down to room temperature, the products were filtered and washed several times with hot deionized water to confirm that the residue of chloride ion (Cl^-) was removed completely. The amount of Cl^- residue was checked by testing with 0.5 mol/L of silver nitrate ($AgNO_3$) reagent; until the white precipitate of AgCl disappeared. The powder products were dried at 90°C overnight.

2.3 | Preparation of $BaZrO_3$ ceramics

There were three sets of samples, consisting of (a) the μm-$BaZrO_3$ original precursor mixed with 5 wt% polyvinyl alcohol (PVA) binder without the sintering aid abbreviated as BZ(SS), (b) the μm-$BaZrO_3$ original precursor mixed with 5 wt% PVA binder and 2 wt% of sintering aid, BZ(SS + SA) and (c) the *sub*-μm $BaZrO_3$ product powders mixed with 5 wt%PVA binder and 2 wt% of sintering aid; BZ(SFA + SA). Notably, the sintering aid that was used in this work is Borosilicate glass; SiO_2–Bi_2O_3–BaO–Li_2O–K_2O nanopowder [IMNG-100(N); Innovative Material and Technical Solution Co., Ltd., Korea]. All the samples; (a), (b), and (c) were pressed into pellets at 150 MPa. All three samples were sintered in air at the same sintering condition of 1400°C for 10 hours with the same heating and cooling rates of 5°C/min.

2.4 | Characterizations

The phase purity and crystal structure were identified by powder X-ray diffraction (XRD; Bruker D8 Advance diffractometer) with CuKα radiation in the 2θ range from 20° to 80° with a 0.02° step size. The lattice parameters was refined by Rietveld analysis of the XRD data, using JANA2006 software.[39] The XRD data for Rietveld refinement were collected on Rigaku, Miniflex600 in the 2θ range from 10° to 120° at 0.02 degree/step. The crystallite size was calculated using Scherrer's equation by applying the full-width at half-maximum (FWHM) of the characteristic peak, according to Equation (1):

$$D_{XRD} = \frac{k\lambda}{\beta_{hkl}\cos\theta}, \quad (1)$$

where D_{XRD} is the crystallite size (nm), k is the constant value of 0.89, λ is the X-ray wavelength (0.154 nm), β_{hkl} is the full-width at half-maximum intensity, and θ is the diffraction angle. The phase identification was also characterized by Raman (DXR Raman, Thermo Scientific model with laser operating on 10 μm spot size at 532 nm) and FT-IR (GX FT-IR model, Perkin Elmer).

Microstructural and morphological characterizations were performed by field-emission scanning electron microscope (FE-SEM, Hitachi 54700 model) and transmission electron microscope (TEM; JEOL-JEM model 2010 operated with 80-200 kV). The Ba:Zr stoichiometric ratio was examined by energy dispersive X-ray (EDX) analysis.

UV-visible (UV-VIS) absorption for $BaZrO_3$ sub-microscale powder was measured using a UV-visible spectrophotometer (T60U, PG instrument). The microwave dielectric measurement was performed using a HP 8719C Vector Network Analyzer dielectric resonator (DR) in the frequency range of 10–11 GHz in transmission mode (S_{21} parameter). The DR puck was placed inside the silver-clad copper resonance cavity on top of low-loss quartz support. The diameter-to-thickness ratio of the DR was adjusted to ~2.26 ± 0.03, in order to ensure that the first resonance mode was of the $TE_{01\delta}$-type. The dielectric constant (ε_r), dielectric loss (tanδ), and unloaded Q-factor were calculated using QWED software. The details of the microwave dielectric measurement are given in.[40]

3 | RESULTS AND DISCUSSION

3.1 | Characterization of $BaZrO_3$ precursors

Phase purity and crystal structure were identified by the powder XRD technique. The XRD peaks were fitted, and the lattice parameter was refined using Rietveld refinement analysis *via* JANA2006 software. The XRD pattern with structural refinement plot is illustrated in Figure 1A; the experimental data are marked as "+" symbols; the red solid line represents the fit, the vertical bars (blue color) represent the expected Bragg reflection positions for cubic $BaZrO_3$, and the green line at the bottom shows the difference between the experimental data and the fit. As a result, all of the XRD peaks could fit well with the standard data from the Inorganic Crystal Structure Database (ICSD) number 97460, which corresponds to the cubic perovskite $BaZrO_3$ (*Pm*3*m* space group). The refinement parameters of the smallest R_{wp} value of 7.14%, and goodness of fitting (GOF) of 1.51 were obtained. The lattice parameter was calculated and found to be 4.1949(3) Å, which is close to the 4.1946 Å in the ICSD. By using Visualization for Electronic and Structural Analysis (VESTA) software, the unit cell representation could be created from the results of refined lattice parameter, as presented in the inset of Figure 1A.

The morphology of μm-$BaZrO_3$ precursor particles was observed by SEM, and the SEM image is illustrated in Figure 1B. It is evident that the μm-$BaZrO_3$ precursor particles

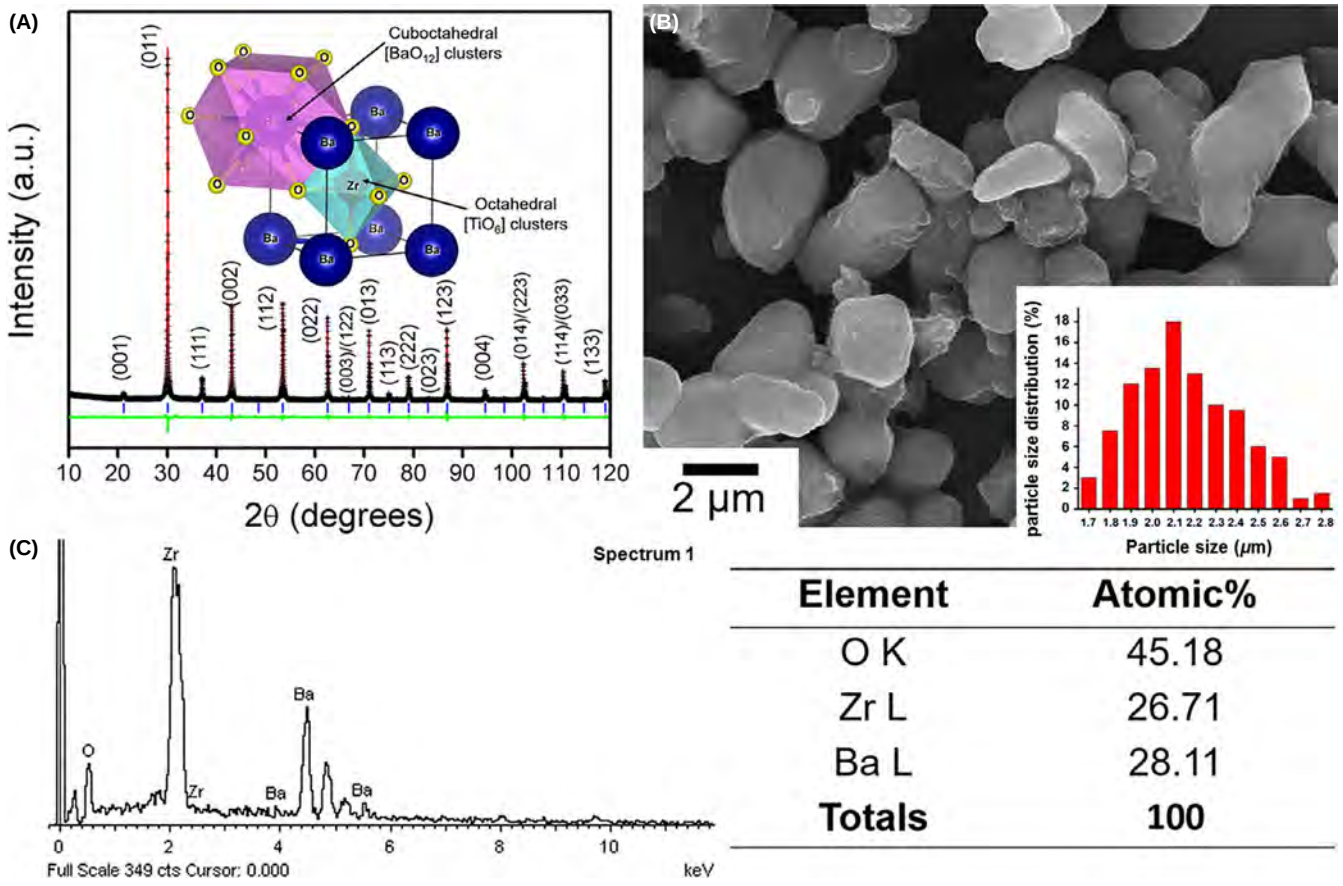

Element	Atomic%
O K	45.18
Zr L	26.71
Ba L	28.11
Totals	**100**

FIGURE 1 (A) Rietveld refinement plot of the XRD pattern, with an inset of schematic unit cell representation of crystalline $BaZrO_3$, which illustrates [BaO_{12}] and [ZrO_6], (B) SEM image with a size distribution histogram and (C) EDX spectrum with a table of O, Zr, and Ba at% for the μm-$BaZrO_3$ precursor prepared from solid-state reaction [Color figure can be viewed at wileyonlinelibrary.com]

contained non-uniform irregular shape with an average particle size of about 1.1 ± 0.9 μm. The Ba:Zr stoichiometric ratio was examined by EDX analysis. The histogram results with atomic% of Ba, Zr, and O atoms are shown in Figure 1C. The analyzed composition indicated an average atomic ratio of Ba/Zr = 1.05.

3.2 | Effect of Reaction temperature on morphology and phase stabilization

Phase purity and crystal structure of the $BaZrO_3$ powder products were checked and compared with the μm-$BaZrO_3$ precursor after the salt flux dissolution (SFD) process at various temperatures from 800°C-1200°C for 4 hours. The XRD patterns are shown in Figure 2. The unit cell parameter was calculated, with the resulting value not being significantly different, as tabulated in Table 1. It can be seen that all samples show the XRD pattern of cubic perovskite $BaZrO_3$ as the predominant phase. It is notable that the single phase could be obtained at only 800°C, 900°C, and 1000°C, and neither $BaCO_3$ nor m-ZrO_2 could be observed. The secondary phases were formed after increasing the reaction temperature to 1200°C. Small traces of orthorhombic

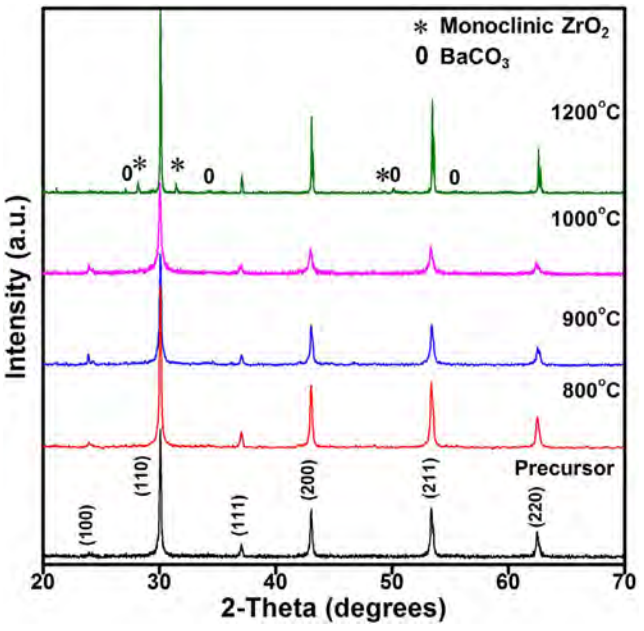

FIGURE 2 XRD patterns of the $BaZrO_3$ powder products obtained from the SFD method at different temperatures of 800°C-1200°C compared to that of the μm-$BaZrO_3$ precursor [Color figure can be viewed at wileyonlinelibrary.com]

Temperature (°C)	Lattice parameter $a = b = c$ (Å)	Crystalline size (nm)	Average particle size (nm)
μm-$BaZrO_3$ precursor	4.1949 (3)	235.7	2.1 ± 0.9 μm
800	4.1943 (1)	97.8	454 ± 152
900	4.1942 (2)	88.3	422 ± 121
1000	4.1941 (4)	76.4	168 ± 23
1200	4.1942 (3)	186.1	170 ± 27
ICSD 97460	4.1946	—	—

TABLE 1 Lattice parameter, crystalline size and average particle size of the μm-$BaZrO_3$ precursor and powder products synthesized at various temperatures for 4 hrs

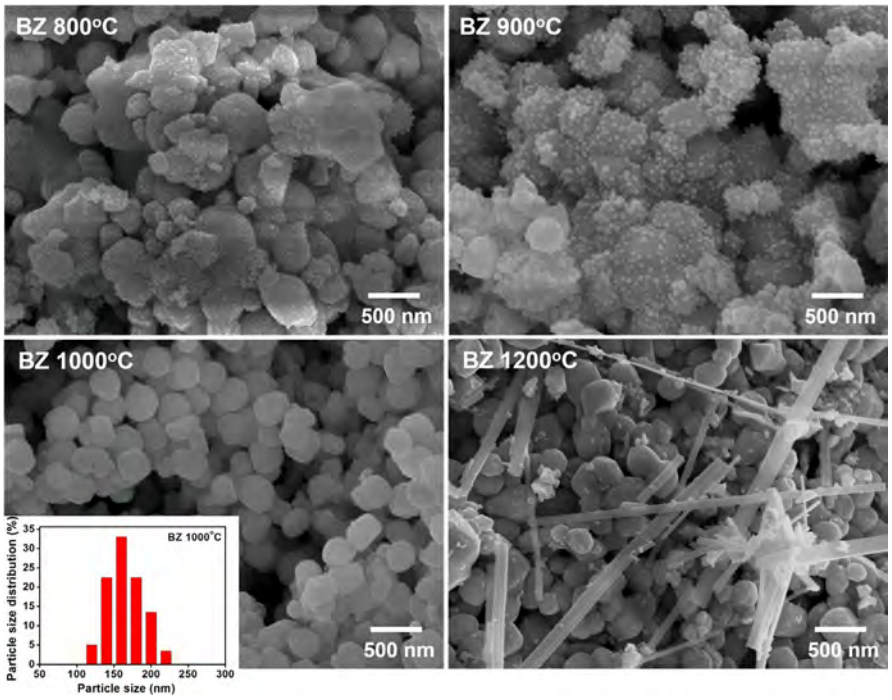

FIGURE 3 SEM images of the $BaZrO_3$ powder products at different temperatures of 800°C-1200°C obtained from the SFD method [Color figure can be viewed at wileyonlinelibrary.com]

$BaCO_3$ with *Pmcn* space group (indexed by an open circle), and monoclinic ZrO_2: m-ZrO_2 with *P*21/*c* space group (indexed by a star), were observed, thus attributing them to the stoichiometric deviation of Ba:Zr from 1:1 (Figure 2). The XRD peaks of $BaCO_3$ and m-ZrO_2 corresponded to the standard data of JCPDS number 71-2394 and 07-0343, respectively. This result means that the reaction temperature of 1200°C was too high. The peak intensity, marked as the $BaZrO_3$ phase, is decreased with increasing reaction temperature from 800°C to 1000°C, which relates to decreasing crystallinity. Furthermore, the XRD peaks broaden with increasing temperature from 800°C to 1000°C, which corresponds to decreasing crystallite size. The crystallite sizes were found to be 97.8, 88.3, and 76.4 nm for 800°C, 900°C, and 1000°C, respectively. The results are listed in Table 1. In addition, the single phase of the $BaZrO_3$ product at 1000°C/4 h was also supported by the Raman and FT-IR spectroscopy. The results are illustrated in the supporting information 1 (Figure S1).

The effect of reaction temperature on the particle morphology of $BaZrO_3$ powder products was studied by SEM. The SEM images are illustrated in Figure 3. As mentioned in Figure 1, the starting μm-$BaZrO_3$ particles were of non-uniform irregular shape with an average particle size of 1.1 ± 0.9 μm. After heating at 800°C for 4 hours, the non-uniform particles could still be observed; however, the particle size of the μm-$BaZrO_3$ precursor was reduced to 454 ± 152 nm. It was noticeable that tiny particles of about 5-10 nm also could be observed, which illustrated the occurrence of bimodal size distribution in this condition. The μm-$BaZrO_3$ particles were reduced to 422 ± 121 nm as well as the tiny particles continuously grow with increasing temperature to 900°C. However, the bimodal size distribution between μm-$BaZrO_3$ and primary particles could still be observed. The particle shape and size were changed totally when the temperature was increased to 1000°C. The irregular shape of μm-$BaZrO_3$ became nearly spherical with dramatically decreasing of

the average particle size to 168 ± 23 nm. It was important that the narrow size distribution could be obtained. A large difference occurred when the temperature was increased to 1200°C. Two kinds of morphologies were observed. The SEM image clearly showed several needle-shaped particles, which were distinguishable from the major spherical ones. These needle-shaped particles resemble the particle morphology of commercial $BaCO_3$, which has been described by other studies.[41] The EDS analysis result also suggests some barium loss (Ba/Zr is ~0.8) on the spherical $BaZrO_3$ particle product at 1200°C as shown in the supporting information (Figure S2), which expected to occur at high temperature or long soaking time. On the other hand, by taking the XRD results (Figure 2) into account, nearly spherical particles can be assigned to $BaZrO_3$, and the needle-shaped ones probably correspond to $BaCO_3$. Therefore, we suggest that 1000°C is the optimum temperature for obtaining $BaZrO_3$ nanoscale products. In addition, the particle morphology of the $BaZrO_3$ product at 1000°C was also observed by TEM. It shows the nearly spherical shape of particle with the average particle size of 68 ± 5 nm. The particle size observed by TEM images are smaller than that from the SEM images (Figure 3), indicating to the polycrystalline-like nature of the $BaZrO_3$ product particles. The TEM images are shown in supporting information (Figure S3).

Since deviation from stoichiometry and deficient local structure can affect properties, these factors could become more crucial during the synthesis. The stoichiometric ratio of Ba:Zr in the nm-$BaZrO_3$ product in this study was well confirmed by using EDX analysis. The analytical result indicated in Figure 4 shows that the atomic ratio of Ba/Zr is equal to 1.02, which is close to the 1.05 Ba/Zr ratio from the μm-$BaZrO_3$ precursor, as mentioned earlier. Therefore, it is worth noting that after the surface modification process with the molten salt, the *sub*-μm-$BaZrO_3$ product particles can maintain the stoichiometric composition close to 1:1 for Ba:Zr, which is similar to that in the μm-$BaZrO_3$ original precursor. The composition control has advantages over synthesis *via* soft-chemical methods in that the final Ba:Zr stoichiometric ratio might deviate from 1:1 due to the different dissolution rate of Ba^{2+} and Zr^{4+} cations.[30]

3.3 | Effect of Reaction Time on Morphology and Phase Stabilization

Figure 5 shows XRD patterns of the μm-$BaZrO_3$ original particles and powder products after heating at 1000°C, in a range of times from 3 minutes to 48 hours. Results of the X-ray analysis confirmed that the single phase of $BaZrO_3$ stabilized from 3 minutes to 12 hours in the cubic crystal structure of the powder products. An insignificant difference in lattice parameters at different dissolution times was observed, according to the list in Table 2. Both orthorhombic $BaCO_3$ and monoclinic ZrO_2 were found as secondary phases when the reaction time was longer than 12 hours.

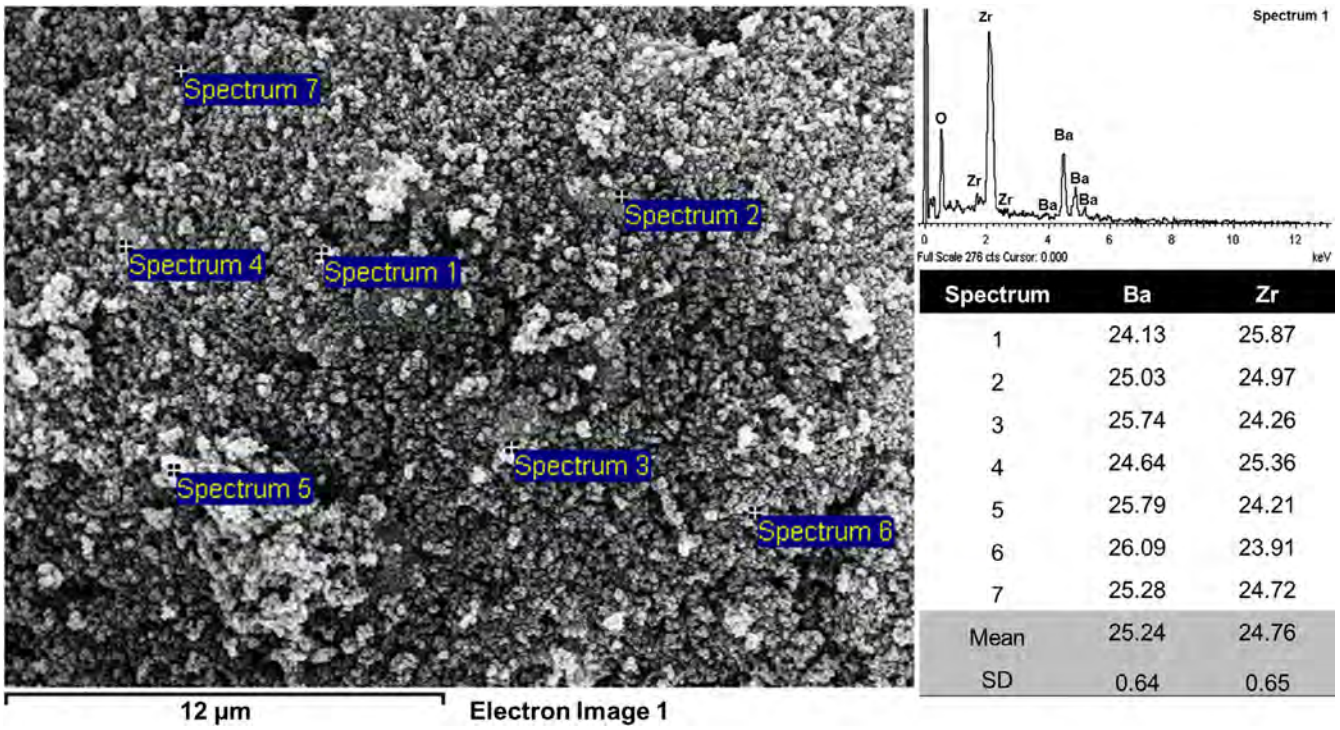

Spectrum	Ba	Zr
1	24.13	25.87
2	25.03	24.97
3	25.74	24.26
4	24.64	25.36
5	25.79	24.21
6	26.09	23.91
7	25.28	24.72
Mean	25.24	24.76
SD	0.64	0.65

FIGURE 4 SEM image with EDX analysis of the $BaZrO_3$ powder product from the SFD method at 1000°C/4 h [Color figure can be viewed at wileyonlinelibrary.com]

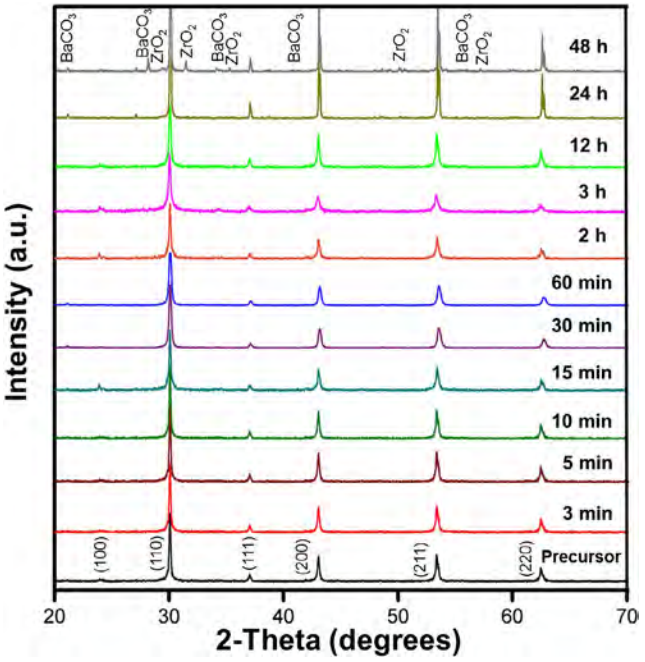

FIGURE 5 XRD patterns of the $BaZrO_3$ powder products after the SFD method at 1000°C for various soaking times compared to that of the μm-$BaZrO_3$ precursor [Color figure can be viewed at wileyonlinelibrary.com]

TABLE 2 Lattice parameter and average particle size of the μm-$BaZrO_3$ precursor and powder products synthesized at 1000°C for various times

Time	Lattice parameter $a = b = c$ (Å)	Average particle size (nm)
μm-$BaZrO_3$ precursor	4.1949 (3)	2.1 ± 0.9 μm
3 min	4.1951 (1)	1.4 ± 1.1 μm
5 min	4.1953 (2)	351 ± 115
15 min	4.1958 (5)	—
30 min	4.1956 (3)	—
60 min	4.1952 (6)	184 ± 51
2 h	4.1949 (3)	179 ± 66
3 h	4.1951 (4)	170 ± 53
4 h	4.1941 (4)	168 ± 23
12 h	4.1943 (6)	236 ± 131
24 h	4.1947 (2)	230 ± 91
48 h	4.1949 (5)	—
ICSD 97460	4.1946	—

The formation mechanism was studied by using SEM to examine time-dependence of the particle size. As a result of the time-resolved experiment, the evolution of particle morphology was revealed, as illustrated in Figure 6. The average particle size for all samples is reported in Table 2. Based on the proposed mechanism from our previous work,[38] the results are discussed briefly relating to that report. Salt flux dissolution method is started by precursor particles being dissolved on the whole surface area *via* action of the NaCl + KCl salt flux, until achieving the optimum or specific size of nanoproduct particles. Then, the oriented-attachment growth of particles took place, which increased the particle size to form non-uniform irregular morphology [38]. Figure 6 shows that the average particle size of μm-$BaZrO_3$ precursors was reduced slightly at 3 minutes from 2.1 ± 0.9 μm to 1.4 ± 1.1 μm. The precursor particles were reduced continuously at 5 minutes, resulting in a sharply decreasing average particle size to 351 ± 115 nm. It is noteworthy that many tiny particles of about 5-10 nm could be observed. It can be understood that after the μm-$BaZrO_3$ precursor and excess eutectic NaCl + KCl salt are heated over 658°C (melting point of the eutectic NaCl + KCl salt,)[42,43] the mixed chloride salt melts completely and attacks the μm-$BaZrO_3$ precursor particle over all directions starting from the surface. As polycrystal normally contains many typical defects, ie stacking faults, twins, and orientation loss, those areas can be attacked easily. Once the particle surface is attacked, the dissolution process starts. The plausible mechanism model was discussed in detail in previous work of these authors, as reported elsewhere.[38] When the dissolution process occurred, several positions on the precursor's surface were dissolved by salt-flux to form as precursor ions (Ba^{2+} and Zr^{4+}) in molten NaCl + KCl salt. However, it can be seen that each region on the surface of original particles has a slightly different dissolution rate resulted in bimodal size distribution of the particle products, as seen in Figure 6. It was important that the dissolution process could maintain the original stoichiometric composition of the μm-$BaZrO_3$ precursor particles. The atomic ratio of Ba/Zr ≈ 1 for the $BaZrO_3$ at 5 minutes was confirmed by EDX analysis, as shown in supporting information (Figure S4). By increasing the time further to 3 hours, the dissolution process continued, and resulted in (a) particle size reduction of the μm-$BaZrO_3$ precursor, (b) higher number of *sub*-μm or nm original particles from the fall out from the agglomerated μm-$BaZrO_3$ precursor, (c) an increasing of concentration of Ba^{2+} and Zr^{4+} precursor ions and (d) particle's shape becoming spherical and uniform. However, it could be seen that, in the initial stage of the dissolution process, the average particle size decreases significantly with a fast rate. Nevertheless, after 60 minutes of the dissolution process, the rate of decrease in average particle size slow down compared to the initial stage. The lower decreasing rate in the 60 minutes to 2 hours of dissolution process may be caused by the increasing of the concentration of Ba^{2+} and Zr^{4+} ion in the NaCl + KCl salt flux close to the saturation state.

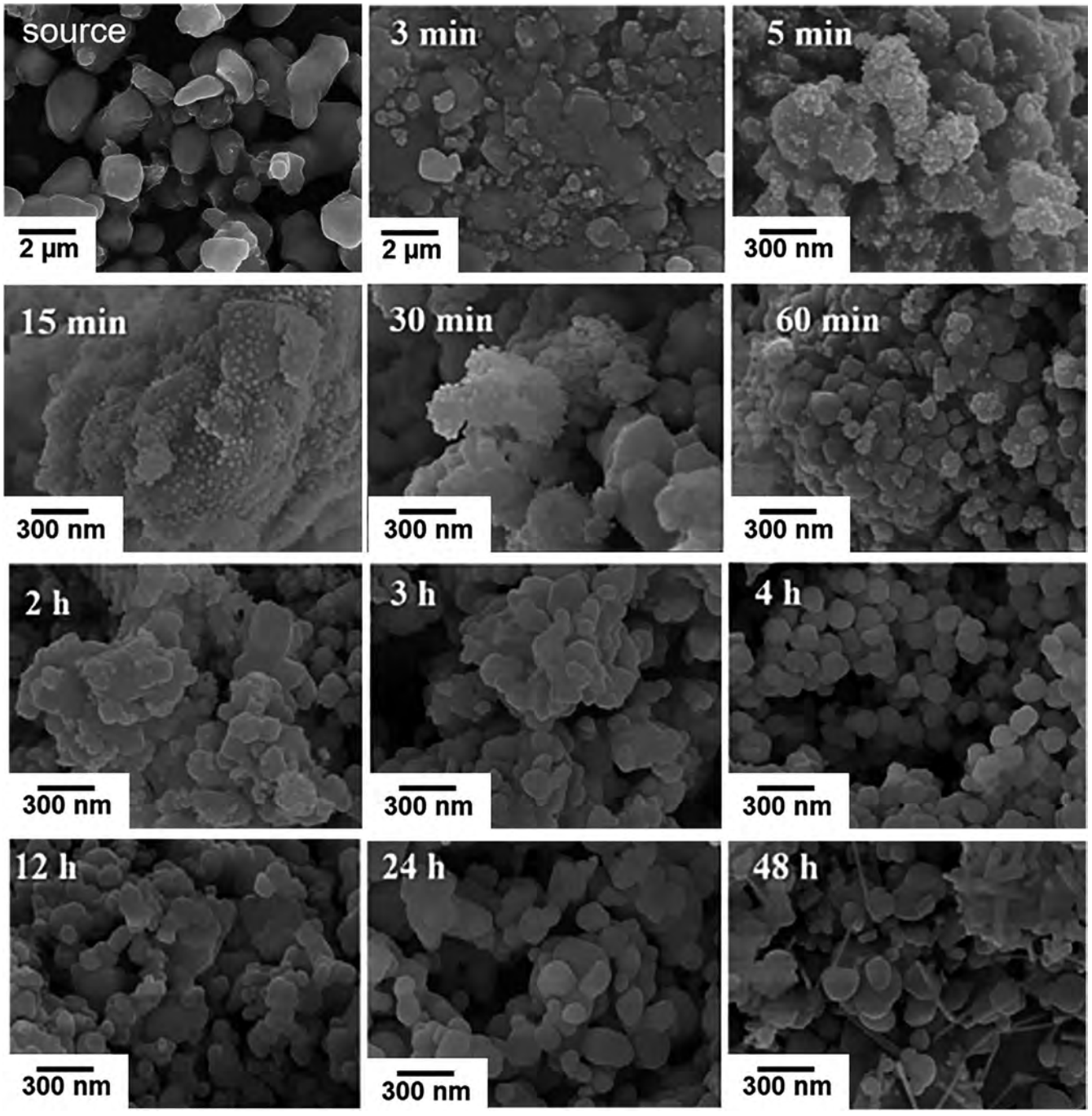

FIGURE 6 SEM images of the μm-$BaZrO_3$ precursor and $BaZrO_3$ particle products after the SFD method at 1000°C for various soaking times (SEM images of the μm-$BaZrO_3$ precursor and $BaZrO_3$ product at 3 min are shown at different magnifications)

The solubility limit of Ba^{2+} and Zr^{4+} ion in the NaCl + KCl system is still unclear and needs further studies. The optimum particle size is reached at 4 hours, when the morphology becomes uniform. The monodispersed $BaZrO_3$ particles can be obtained with an average particle size of about 168 ± 23 nm. These particles are nearly spherical in shape, as demonstrated in Figure 6. It is interesting that up to this time, the *sub*-μm-$BaZrO_3$ particle products still maintained original stoichiometry of the μm-$BaZrO_3$ precursor. The result of EDX analysis was mentioned earlier in Figure 4. After 12 hours, the uniform morphology was destroyed by particle agglomeration. The average particle size increased to 236 ± 131 and 230 ± 91 nm at 12 and 24 hours, respectively, with broad size distribution. The mechanism at this stage was consistent with rapid self-nucleation from the supersaturated solution, according to the La-Mer mechanism diagram.[44] Nucleated particles, which are called "*secondary particles*", deposit on the surface of existing original-particles. The primary (original) and secondary particles could agglomerate, fuse and grow using

the oriented attachment (OA) mechanism, which involves spontaneous self-organization of contact particles by sharing a common crystallographic orientation. The adjacent particles join together and generally become bigger with irregular morphology.[38,45] At this stage, the Ba:Zr stoichiometric ratio deviates from the original stoichiometry of the μm-precursor particle. The EDX analysis result for $BaZrO_3$ at 24 hours showed evidence of Zr-rich stoichiometric composition of Ba/Zr ≈ 0.76, as evidenced in supporting information (Figure S5), because the Zr^{4+} (B-site) ion precipitated much faster than the Ba^{2+} (A-site) ion. This was due to lower solubility of Zr^{4+}, with Ba^{2+} being taken up into the dissolved particles after Zr^{4+} nucleation.[23] More details on the nucleation and growth mechanism could be explored in our previous work.[33,38]

Different morphologies, observed again by SEM after 48 hours (Figure 6), were similar to the SEM image of the powder product at 1200°C, as mentioned in Figure 3. The needle-shaped particles with a high aspect ratio were attributed to the $BaCO_3$ particles. Occurrence of the $BaCO_3$ and *m*-ZrO_2 phase can be found at 1200°C/4 h, or even 1000°C/48 h, because different solubility of Ba and Zr metal ions makes a totally different nucleation rate during self-nucleation. The EDX analysis of two different areas, which focused on (a) needle-like shape and (b) nearly spherical shape, was investigated, as illustrated in supporting information (Figure S6). It was found that the Ba-rich composition could appear all around the needle-like particle as well as Zr-rich composition appearing on the nearly spherical particle. More confirmation for the appearance of the $BaCO_3$ phase could not be shown by EDX analysis because it is not very sensitive to carbon.

3.4 | Optical properties

$BaZrO_3$ is considered as an important phosphor host material, due to its potential application in different luminescent displays. The optical properties of *sub*-μm-$BaZrO_3$ powder products obtained after 4 h at 1000°C was investigated by UV-visible absorption measurement, and compared to the μm-$BaZrO_3$ original precursor. The energy gap is related to the photon energy and absorbance by the following Equation (2).[46]

$$\alpha h\nu \propto \left(h\nu - E_g\right)^n, \tag{2}$$

where α is the absorbance, h is Plank constant, ν is frequency, E_g is the optical band gap, and the exponent (n) depends on the nature of the observed electronic transition. The electronic transition for $n = 2$ is allowed directly, whereas the $n = ½$ is allowed indirectly. Since zirconates, titanates, and zirconate-titanate compounds have an optical absorption process dominated by direct electronic transition according to the literature,[1,47,48] the $n = 2$ exponent was therefore considered. The relationship between $(\alpha h\nu)^2$ and $h\nu$ (eV) is plotted and shown in Figure 7. The

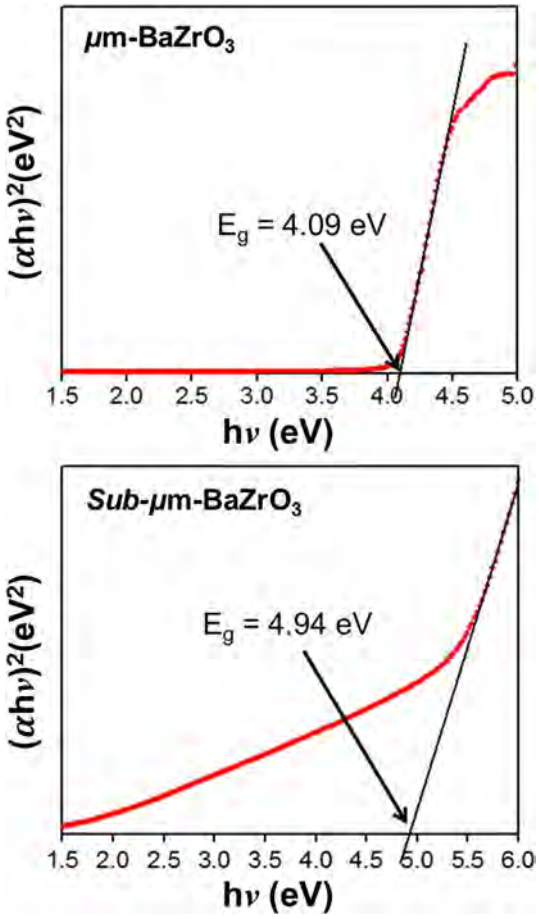

FIGURE 7 Energy gap (E_g) determined from the UV-Vis absorbance spectrum of the *sub*-μm-$BaZrO_3$ powder product obtained from the SFD method at 1000°C compared to that of the μm-$BaZrO_3$ precursor [Color figure can be viewed at wileyonlinelibrary.com]

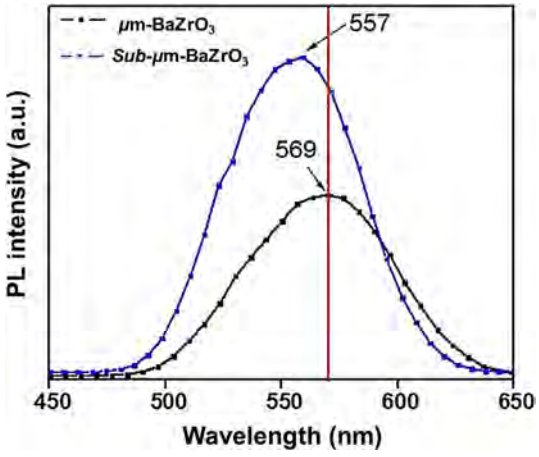

FIGURE 8 Photoluminescence spectra of the *sub*-μm-$BaZrO_3$ powder product from the SFD method at 1000°C compared to those of the μm-$BaZrO_3$ precursor [Color figure can be viewed at wileyonlinelibrary.com]

μm-$BaZrO_3$ precursor exhibits a typically sharp curved band of absorbance, like crystalline materials, while the *sub*-μm-$BaZrO_3$ product shows an absorption behavior similar to that

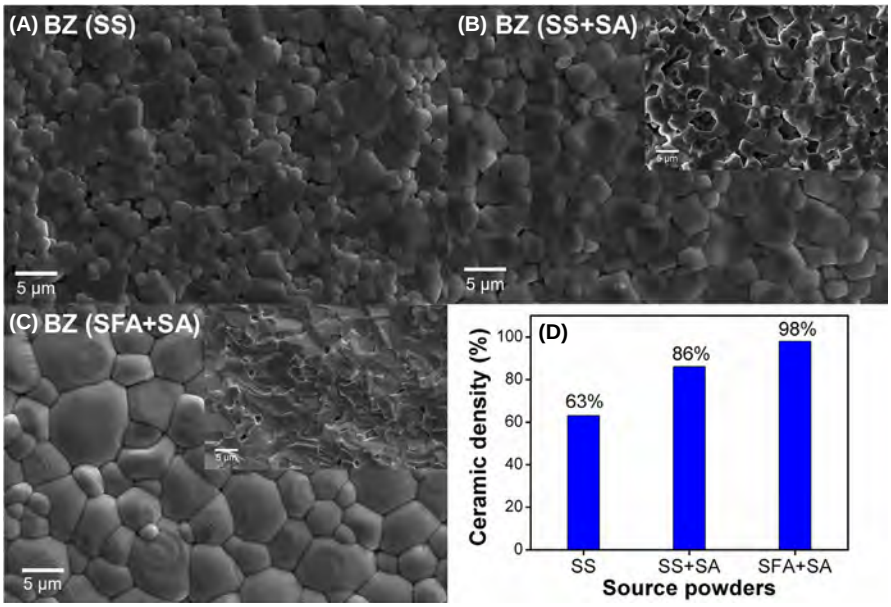

FIGURE 9 SEM images of (A) BZ ceramic from solid-state (SS) source powders, (B) BZ ceramic from solid-state (SS) source powders with using sintering aids (SA), (C) BZ ceramic from salt flux dissolution (SFD) method source powders with using sintering aids (SA), all ceramics were sintered at 1400°C for 10 h [Color figure can be viewed at wileyonlinelibrary.com]

TABLE 3 Microwave dielectric constant and quality factor (Q-factor) of the $BaZrO_3$ ceramic from this study compared to other methods

	Microwave-assisted hydrothermal[1]	Solid-state reaction[56]	Combustion [57]	Soft-mechanochemical[33]	Salt flux dissolution method (this work)
Sintering temperature	1670°C	1650°C	1650°C	1450°C	1400°C
Sintering time	4 h	4 h	2 h	6 h	10 h
ε_r	38.40	35.00	32.23	37.42	37.26
Q-factor	5731	8800	—	5096.91	4387.8

of an amorphous semiconductor.[49] This result is in qualitative agreement with the crystallinity that was mentioned in the XRD results. The energy gap could be estimated by the linear extrapolation of the slope between $(\alpha hv)^2$ and hv. The *sub*-μm-$BaZrO_3$ product shows the optical band gap of 4.94 eV, which is higher than the 4.09 eV of the μm-$BaZrO_3$ precursor. The increase in the *sub*-μm-$BaZrO_3$ energy gap can be ascribed to the reduction of lattice defects (oxygen vacancies), resulting in decreasing intermediate energy levels in the band region of $BaZrO_3$. This result agrees well with the interpretation from Cavalcante *et al.*, in that the optical band gap is controlled by the structural order-disorder degree and also point defects in the $BaZrO_3$ lattice.[49] On the other hand, the increase of energy band gap is also related to the decreasing particle size.[50,51]

Room temperature PL emission spectra of the *sub*-μm-$BaZrO_3$ powder product, in comparison to the μm-$BaZrO_3$ precursor after excitation at 350.7 nm (3.52 eV), are displayed in Figure 8. The intense blue-green PL spectra, with maximum emission at around 568 and 557 nm for nm- and μm-$BaZrO_3$, respectively, are associated with structural order-disorder degrees or point defects in the $BaZrO_3$ lattice, which sheds light on the structural deformation effects in the electronic structure. Cavalcante et al.[49] reported typical PL emission of disordered $BaZrO_3$ at ~540 nm, and

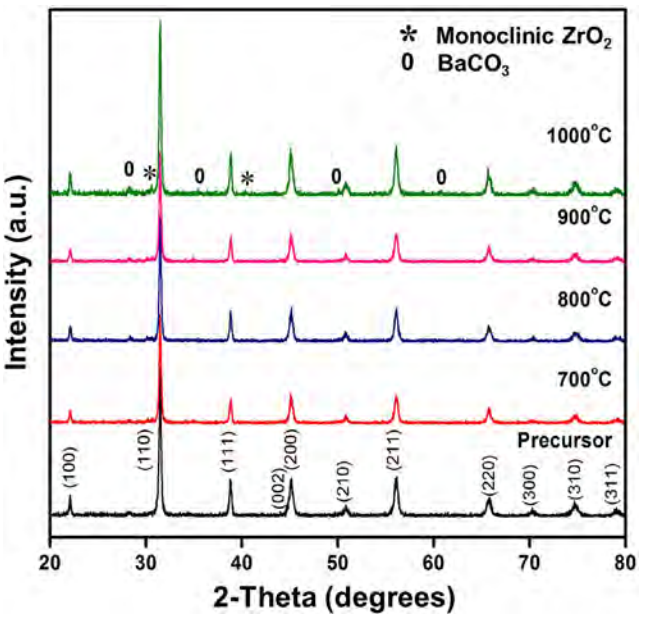

FIGURE 10 XRD patterns of the 0.87BT-0.13BZ-CT precursor powder compared to those of the 0.87BT-0.13BZ-CT powder products obtained from the SFD method at different temperatures of 700°C-1000°C [Color figure can be viewed at wileyonlinelibrary.com]

Leite et al.[52] reported ~585 nm of the same material by using the same excitation wavelength. These blue-green emissions are also related directly to the oxygen deficiency created in the host of the $BaZrO_3$ lattice ($BaZrO_{3-\delta}$). Mostly, the $BaZrO_{3-\delta}$ can create complex local defects of oxygen vacancies according to the V_O^x, $V_O^{\cdot}$, and $V_O^{\cdot\cdot}$ Kröger-Vink notation.[49,53] Neutral V_O^x captures two electrons ↑↓, singly ionized $V_O^{\cdot}$ captures one electron ↑ and double ionized $V_O^{\cdot\cdot}$ has no trapped electrons. However, Dhahri et al.[54] have proved that the presence of $V_O^{\cdot\cdot}$ allows the formation of intermediary energy levels in the band gap, leading to a blue-green emission. The electronic defects can be represented as follows:

$$[ZrO_6] \rightarrow [ZrO_5] \cdot V_O^{\cdot\cdot} + 1/2O_2 + 2e^- \quad (3)$$

Different research also has found that PL intensity is related directly to the particle size. In that cases, the PL intensity increases when the particle size decreases, as a result of quantum effects.[45] It is clear that *sub*-μm-$BaZrO_3$ exhibits higher PL intensity (blue line) when compared to μm-$BaZrO_3$ intensity (black line). The blueshift of maximum PL peak is attributed to the spherical shape of the particle.[45,53]

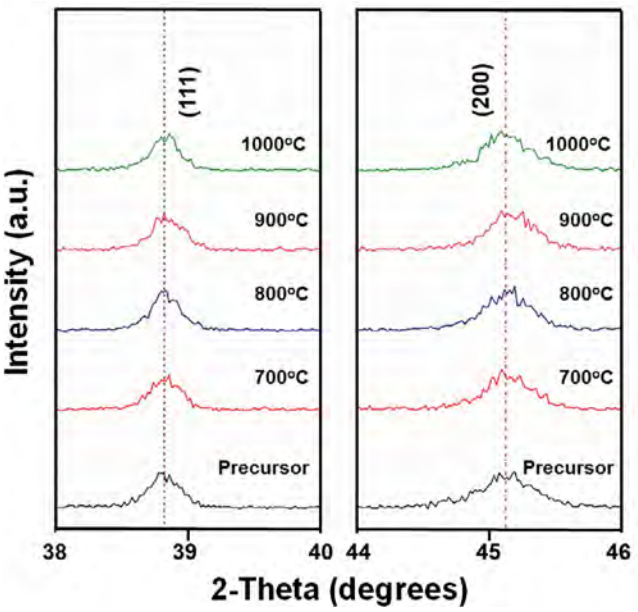

FIGURE 11 Enlarged plot of the XRD pattern for the (111) and (200) peaks of the 0.87BT-0.13BZ-CT precursor powder compared to those of the 0.87BT-0.13BZ-CT powder products obtained from the SFD method at different temperatures of 700°C-1000°C [Color figure can be viewed at wileyonlinelibrary.com]

3.5 | Microwave dielectric properties

Since achieving fully dense ceramic (≥98%), as required for all applications, the *sub*-μm-$BaZrO_3$ obtained by salt flux dissolution method was used in this study as the source of powder and sintered at 1400°C for 10 hours that is lower than the 1650°C in normal case.[54] The $BaZrO_3$ ceramic had a relative density of 98.5% and average grain size of about 4.45 ± 3.50 μm. The surface of ceramic and microstructure of the fractured cross-section showed well-defined grain and grain boundaries with excellent connectivity from grain to grain, as illustrated in Figure 9, comparison to $BaZrO_3$ ceramics from other methods of source powders. It can be seen that the ceramic obtained from solid-state reaction (SS) powder showed the lowest density. With using the sintering aids, the density could be improved from ~63% to ~84%. Interestingly, using the powder obtained from the salt flux dissolution (SFD) method, the ceramic density could be improved to ~98%.

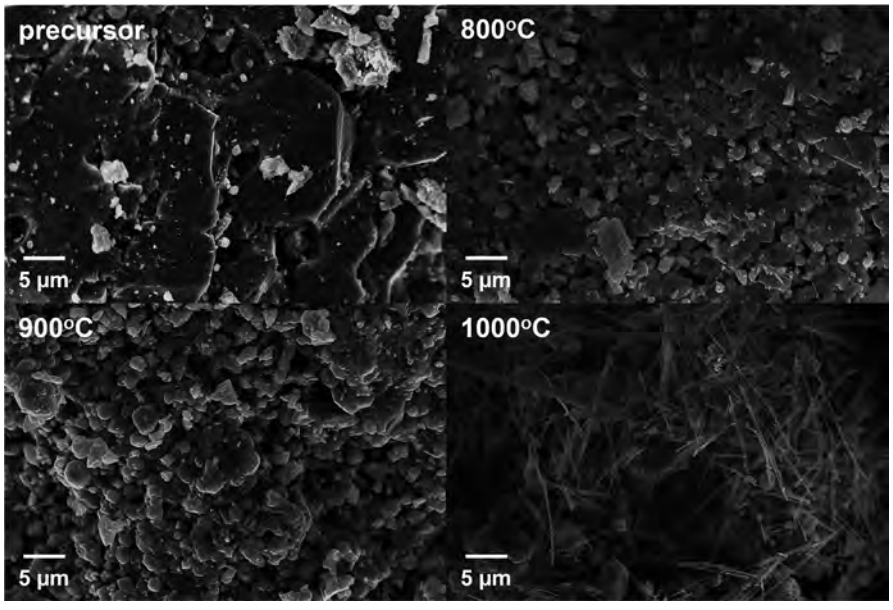

FIGURE 12 SEM images of the 0.87BT-0.13BZ-CT product particles obtained from the SFD method at different temperatures of 800°C-1000°C compared to those of the micron-size precursor

Diameter and thickness of the ceramic sample for microwave measurements were 5.54 and 2.85 mm, respectively. The resonance frequency (f_0) was 8974.9 MHz and FWHM (at 3 dB attenuation) was 17.4 MHz. The loaded quality factor (Q_L) was calculated to be 585. The dielectric constant (ε_r) of 37.3, dielectric loss (tan δ) of 2.045×10^{-3}, unloaded quality factor (Q_U) of 489, and the product of resonance frequency and quality factor ($Q_U \times f_0$) of 4388 GHz were obtained using the QWED software. The microwave dielectric constant obtained from this study was similar to that reported in the literature,[1,55,56] as can be seen in Table 3.

3.6 | Micro-to-nanoscale conversion of $0.87BaTiO_3$–$0.13BaZrO_3$–$CaTiO_3$ powder

$BaZrO_3$ can be a precursor for binary or ternary perovskite oxide lead-free piezoelectric materials, which exhibit excellent piezoelectric properties; therefore, it has the opportunity of replacing lead-based piezoelectric materials. This study also applied the SFD method to convert the micron-size particles in the lead-free $0.87BaTiO_3$–$0.13BaZrO_3$–$CaTiO_3$ (0.87BT–0.13BZ-CT) system. The 0.87BT–0.13BZ-CT precursor was prepared by solid-state reaction at 1300°C/4 h. This composition was selected from a previous work by these authors because it could exhibit a high piezoelectric strain coefficient $\left(d_{33}^*\right)$ of about 1030 pm/V at 10 kV.[57] The SFD process was performed using eutectic NaCl + KCl at various reaction temperatures from 700°C to 1000°C. Phase purity was identified by the XRD technique, resulting in the XRD pattern illustrated in Figure 10. It was found that 0.87BT–0.13BZ-CT powder products, at 700°C, 800°C, and 900°C, are single phase similar to the XRD pattern of the 0.87BT–0.13BZ-CT precursor. Nevertheless, the secondary phase of $BaCO_3$ and m-ZrO_2 could be observed when the reaction temperature reached 1000°C. This result means that the reaction temperature of 1000°C was too high for obtaining the single phase of the 0.87BT–0.13BZ-CT system.

The XRD peak position at (111) and (200) reflection did not shift, according to the enlarged plot in 2θ range of 38°-40° and 44°-46°, respectively, in Figure 11. The detailed characterization of the crystal structure for 0.87BT–0.13BZ-CT systems was described elsewhere.[57] It was surprising that when the SEM image of the powder was considered at 900°C, the large micron-size particles of >10 μm could be reduced to the specific particle size of around 2.8 ± 0.4 μm, with more uniform particle morphology, as shown in the SEM images in Figure 12. This result indicated that the large particle size of 0.87BT–0.13BZ-CT powder could be reduced successfully by the SFD method. It can be suggested that the specific size regime is dependent on the starting particle size of the micron-size precursor. However, the needle-like shape of the $BaCO_3$ phase in this system became evident at 1000°C, which is similar to the observation of the SEM image of $BaZrO_3$. Overall, it is reasonable to assume that the critical conditions (for example; reaction temperature, time, type, and amount of eutectic salt) are needed to be controlled to achieve a morphological transformation into nearly spherical shape and smallest particle size.

4 | CONCLUSIONS

This research shows the direct conversion of micro-to-nanoscale particles as a convenient technique by using the SFD method for achieving uniform perovskite $BaZrO_3$ powders. On the basis of the SFD process, a large micron-size particle was reduced drastically to sub-micrometer as well as nanometer particles by controlling the reaction time and temperature. In terms of optimum overall reaction, the irregular morphology of particles could be transformed to nearly spherical, and the broad size distribution became narrow. More importantly, highly accurate stoichiometry should be the key factor considered, besides the desired shape and size of monodispersed particles in the nanoscale preparation. This novel preparation route could provide the final product without changing the stoichiometry or crystal structure. The advantages of this method, which is fast, reproducible and inexpensive, and easily scaled-up for obtaining uniform sub-micron or nanoscale particles can be proved.

ACKNOWLEDGMENTS

This research was supported by KMITL under grant no A118-0361-005 and 2562-01-05-46. The work of T.C. was supported by KMITL under grant no. KREF146201. The work of T.K. was supported by internal NIMS project funds PA5160 and PA4020. N.V. and T.K. acknowledge the KMITL under "Academic Melting-Pot program" under grant no. KREF206203.

ORCID

Taras Kolodiazhnyi https://orcid.org/0000-0002-9630-9461

Naratip Vittayakorn https://orcid.org/0000-0001-9245-0639

REFERENCES

1. Parida S, Rout SK, Cavalcante LS, Sinha E, Li MS, Subramanian V, et al. Structural refinement, optical and microwave dielectric properties of $BaZrO_3$. Ceram Int. 2012;38(3):2129–38.
2. Korotcenkov G, Han SD, Stetter JR. Review of electrochemical hydrogen sensors. Chem Rev. 2009;109(3):1402–33.
3. Fluri A, Marcolongo A, Roddatis V, Wokaun A, Pergolesi D, Marzari N, et al. Enhanced proton conductivity in Y-doped $BaZrO_3$ *via* strain engineering. Adv Sci. 2017;4(12):1700467–77.

4. Lyagaeva J, Danilov N, Vdovin G, Bu J, Medvedev D, Demin A, et al. A new Dy-doped $BaCeO_3$–$BaZrO_3$ proton-conducting material as a promising electrolyte for reversible solid oxide fuel cells. J Mater Chem A. 2016;4(40):15390–9.
5. Chaiyo N, Cann DP, Vittayakorn N. Lead-free (Ba, Ca)(Ti, Zr)O_3 ceramics within the polymorphic phase region exhibiting large, fatigue-free piezoelectric strains. Mater Des. 2017;133:109–21.
6. Celik E, Mutlu IH, Hascicek YS. Sol-gel processing of buffer layers on Ni tape for YBCO surface coated conductors. IEEE Trans Appl Supercond. 2000;10(1):1162–5.
7. Athayde DD, Souza DF, Silva AMA, Vasconcelos D, Nunes EM, Costa JC, et al. Review of perovskite ceramic synthesis and membrane preparation methods. Ceram Int. 2016;42(6):6555–71.
8. Pan L, ZhuG, Atta NF, GalalA, et al. Perovskite nanomaterials—synthesis, characterization, and applications; ch. 4. In: PanL, ZhuG, editors. Perovskite materials—synthesis, characterisation, properties, and applications. London: Intech, 2016; p. 107–151
9. Sin A, Montaser B, Odier P, Weiss F. Synthesis and sintering of large batches of barium zirconate nanopowders. J Amer Ceram Soc. 2004;85(8):1928–32.
10. Azad AM, Subramaniam S. Synthesis of $BaZrO_3$ by a solid-state reaction technique using nitrate precursors. Mater Res Bull. 2002;37(1):85–97.
11. Schaak RE, Mallouk TE. Perovskites by fesign: a toolbox of solid-state reactions. Chem Mater. 2002;14(4):1455–71.
12. Zou Y, Luo Y, Wen N, Ye T, Xu C, Yu J, et al. Fabricating $BaZrO_3$ hollow microspheres by a simple reflux method. New J Chem. 2014;38(6):2548–53.
13. Lavand AB, Malghe YS. Synthesis of nanosized $BaZrO_3$ from oxalate precursor. J Therm Anal Calorim. 2014;118(3):1613–8.
14. Gonçalves MD, Muccillo R. Properties of yttrium-doped barium zirconate ceramics synthesized by the oxidant-peroxo method. Ceram Int. 2014;40(1):911–7.
15. Taglieri G, Tersigni M, Villa PL, Mondelli C. Synthesis by the citrate route and characterisation of $BaZrO_3$, a high tech ceramic oxide: preliminary results. Int J Inorg Mater. 1999;1(1):103–10.
16. Khort AA, Podbolotov KB. Preparation of $BaTiO_3$ nanopowders by the solution combustion method. Ceram Int. 2016;42(14):15343–8.
17. Khaliullin SM, Zhuravlev VD, Bamburov VG. Solution-combustion synthesis of $MZrO_3$ zirconates (M = Ca, Sr, Ba) in open reactor: Thermodynamic analysis and experiment. Int J Self Propag High Temp Synth. 2017;26(2):93–101.
18. Kanie K, Seino Y, Matsubara M, Nakaya M, Muramatsu A. Hydrothermal synthesis of $BaZrO_3$ fine particles controlled in size and shape and fluorescence behavior by europium doping. New J Chem. 2014;38(8):3548–55.
19. Kanie K, Seino Y, Matsubara M, Muramatsu A. Size-controlled hydrothermal synthesis of monodispersed $BaZrO_3$ sphere particles by seeding. Adv Powder Technol. 2017;28(1):55–60.
20. Lu Z, Tang Y, Chen L, Li Y. Shape-controlled synthesis and characterization of $BaZrO_3$ microcrystals. J Cryst Growth. 2004;266(4):539–44.
21. Veith M, Mathur S, Lecerf N, Huch V, Decker T, Beck HP, et al. Sol-Gel synthesis of nano-scaled $BaTiO_3$, $BaZrO_3$ and $BaTi_{0.5}Zr_{0.5}O_3$ oxides *via* single-source alkoxide precursors and semi-alkoxide routes. J Solgel Sci Technol. 2000;17(2):145–58.
22. Yoko A, Akizuki M, Oshima Y. Formation mechanism of barium zirconate nanoparticles under supercritical hydrothermal synthesis. J Nanopart Res. 2014;16(4):2330–5.
23. Yoko A, Akizuki M, Umezawa N, Ohno T, Oshima Y. Growth of $Ba_{1-x}Sr_xZrO_3$ ($0 \leq x \leq 1$) nanoparticles in supercritical water. RSC Adv. 2016;6(72):67525–67233.
24. Liu S, Huang L, Li W, Liu X, Jing S, Li J, et al. Green and scalable production of colloidal perovskite nanocrystals and transparent sols by a controlled self-collection process. Nanoscale. 2015;7(27):11766–76.
25. Suematsu K, Arimura M, Uchiyama N, Saita S, Makino T. High-performance dielectric thin film nanocomposites of barium titanate and cyanoethyl pullulan: controlling the barium titanate nanoparticle size using a sol-gel method. RSC Adv. 2016;6(25):20807–13.
26. Borja-Urby R, Diaz-Torres LA, Garcia-Martinez I, Bahena-Uribe D, Casillas G, Ponce A, et al. Crystalline and narrow band gap semiconductor $BaZrO_3$: Bi–Si synthesized by microwave–hydrothermal synthesis. Catal Today. 2015;250:95–101.
27. Nguyen-Phan TD, Huy CN, Kim CK, Shin EW. Facile microwave-assisted synthesis and controllable architecture of three-dimensional nickel titanate. Cryst Eng Comm. 2015;17(24):4562–74.
28. Aghayan M, Khorsand A, Behdani M, Hashim A. Sol–gel combustion synthesis of Zr-doped $BaTiO_3$ nanopowders and ceramics: dielectric and ferroelectric studies. Ceram. Int. 2014;40(10):16141–6.
29. Rabuffetti FA, Brutchey RL. Complex perovskite oxide nanocrystals: low-temperature synthesis and crystal structure. Dalton Trans. 2014;43(39):14499–513.
30. Yoko A, Akizuki M, Hirao N, Kohara S, Kumar M, Umezawa N, et al. *In-situ* x-ray diffraction for millisecond-order dynamics of $BaZrO_3$ nanoparticle formation in supercritical water. J Supercrit Fluid. 2016;107:746–52.
31. Charoonsuk T, Vittayakorn W, Vittayakorn N, Seeharaj P, Maensiri S. Sonochemical synthesis of monodispersed perovskite barium zirconate ($BaZrO_3$) by using an ethanol–water mixed solvent. Ceram. Int. 2015;41(1):S87–S94.
32. Charoonsuk P, Baitahe R, Vittayakorn W, Atiwongsangthong N, Muanghua R, Seeharaj P, et al. Synthesis of monodispersed perovskite barium zirconate ($BaZrO_3$) by the sonochemical method. Ferroelectrics. 2013;453(1):54–61.
33. Charoonsuk T, Vittayakorn N. Soft-mechanochemical synthesis of monodispersed $BaZrO_3$ sub-microspheres: phase formation and growth mechanism. Mater Des. 2017;117:44–52.
34. Sahu P, Prasad BLV. Fine control of nanoparticle sizes and size distributions: temperature and ligand effects on the digestive ripening process. Nanoscale. 2013;5(5):1768–71.
35. Bhaskar SP, Vijayan M, Jagirdar BR. Size modulation of colloidal Au nanoparticles *via* digestive ripening in conjunction with a solvated metal atom dispersion method: An insight into mechanism. J Phys Chem C. 2014;118(31):18214–25.
36. Moiraghi R, Douglas-Gallardo OA, Coronado EA, Macagno VA, Perez MA. Gold nucleation inhibition by halide ions: a basis for a seed-mediated approach. RSC Adv. 2015;5(25):19329–36.
37. Shaik AH, Chakraborty J. Synthesis of monodisperse copper nanoparticles using a modified digestive ripening technique and formation of superlattices. RSC Adv. 2015;5(104):85974–7.
38. Charoonsuk T, Vittayakorn N. A facile one step conversion of the sub-micrometer to uniform nanopowder in tetragonal $BaTiO_3$ via a surface active etching salt. Mater Des. 2016;110:233–44.
39. Petříček V, Dušek M, Palatinus L. Crystallographic computing system JANA2006: general features. Z Kristallogr Cryst Mater. 2014;229:345–9.

40. Kolodiazhnyi T. Origin of extrinsic dielectric loss in 1:2 ordered, single-phase $BaMg_{1/3}Ta_{2/3}O_3$. J Eur Ceram Soc. 2014;34(7):1741–53.
41. López MCB, Fourlaris G, Rand B, Riley FL. Characterization of barium titanate powders: barium carbonate identification. J Am Ceram Soc. 2004;82(7):1777–86.
42. Zhou H, Mao Y, Wong SS. Probing structure−parameter correlations in the molten salt synthesis of $BaZrO_3$ perovskite submicrometer-sized particles. Chem Mater. 2007;19(22):5238–49.
43. Liu X, Fechler N, Antonietti M. Salt melt synthesis of ceramics, semiconductors and carbon nanostructures. Chem Soc Rev. 2013;42(21):8237–65.
44. LaMer VK, Dinegar RH. Theory, production and mechanism of formation of monodispersed hydrosols. J Am Chem Soc. 1950;72(1):4847–54.
45. Moreira ML, Andrés J, Mastelaro VR, Varela JA, Longo E. On the reversed crystal growth of $BaZrO_3$ decaoctahedron: shape evolution and mechanism. Cryst Eng Comm. 2011;13(19):5818–24.
46. Wood DL, Tauc J. Weak absorption tails in amorphous semiconductors. Phys Rev B. 1972;5(8):3144–51.
47. Gurgel MFC, Espinosa JWM, Campos AB, Rosa ILV, Joya MR, Souza AG, et al. Photoluminescence of crystalline and disordered BTO: Mn powder: Experimental and theoretical modeling. J Lumin. 2007;126(2):771–8.
48. Longo VM, Cavalcante LS, Erlo R, Mastelaro VR, Figueiredo AT, Sambrano JR, et al. Strong violet–blue light photoluminescence emission at room temperature in $SrZrO_3$: Joint experimental and theoretical study. Acta Mater. 2008;56(10):2191–202.
49. Cavalcante LS, Longo VM, Zampieri M, Espinosa JWM, Pizani PS, Sambrano JR, et al. Experimental and theoretical correlation of very intense visible green photoluminescence in $BaZrO_3$ powders. J Appl Phys. 2008;103(6):063527.
50. Avinash BS, Chaturmukha VS, Jayanna HS, Naveen CS, Rajeeva MP, Harish BM, et al. Effect of particle size on band gap and DC electrical conductivity of TiO_2 nanomaterial. AIP Conf Proc. 2016;1728(1):020426.
51. Singh M, Goyal M, Devlal K. Size and shape effects on the band gap of semiconductor compound nanomaterials. J Taibah Univ Sci. 2018;12(4):470–5.
52. Leite ER, Pontes FM, Lee EJH, Aguiar R, Longo E, Pontes DSL, et al. An investigation of metal oxides which are photoluminiscent at room temperature. J Mol Struc- THEOCHEM. 2004;668(2):87–91.
53. Moreira ML, Andrés J, Varela JA, Longo E. Synthesis of fine micro-sized $BaZrO_3$ powders based on a decaoctahedron shape by the microwave-assisted hydrothermal method. Cryst Growth Des. 2009;9(2):833–9.
54. Dhahri K, Bejar M, Dhahri E, Soares MJ, Graça MFP, Sousa MA, et al. Blue-green photoluminescence in $BaZrO_{3-\delta}$ powders. Chem Phys Lett. 2014;610:341–4.
55. Sivasubramanian V, Murthy VRK, Viswanathan B. Microwave dielectric properties of certain simple alkaline earth perovskite compounds as a function of tolerance factor. Jpn J Appl Phys. 1997;36(1):194–7.
56. Kumar HP, Vijayakumar C, George CN, Solomon S, Jose R, Thomas J, et al. Characterization and sintering of $BaZrO_3$ nanoparticles synthesized through a single-step combustion process. J Alloys Compd. 2008;458(1):528–31.
57. Sutapun M, Charoonsuk T, Kolodiazhnyi T, Vittayakorn N. $CaTiO_3$ induced ferroelectric phase coexistence and low temperature dielectric relaxation in $BaTiO_3$–$BaZrO_3$ ceramics. J Am Ceram Soc. 2017;101(5):1957–66.

SUPPORTING INFORMATION

Additional supporting information may be found online in the Supporting Information section at the end of the article.

How to cite this article: Charoonsuk T, Kolodiazhnyi T, Vittayakorn N. The modification of surface, size and shape of barium zirconate powder *via* salt flux. *J Am Ceram Soc*. 2019;102:5772–5785. https://doi.org/10.1111/jace.16495